


Effects of pore interconnectivity on bone regeneration in carbonate apatite blocks

Maab Elsheikh, Ryo Kishida *, Koichiro Hayashi, Akira Tsuchiya, Masaya Shimabukuro and Kunio Ishikawa

Department of Biomaterials, Faculty of Dental Science, Kyushu University, 3-1-1 Maidashi Higashi-ku, Fukuoka 812-8582, Japan

*Correspondence address. Tel: +81-92-642-6346; Fax: +81-92-642-6348; E-mail: kishida@dent.kyushu-u.ac.jp

Abstract

Porous architecture in bone substitutes, notably the interconnectivity of pores, is a critical factor for bone ingrowth. However, controlling the pore interconnectivity while maintaining the microarchitecture has not yet been achieved using conventional methods, such as sintering. Herein, we fabricated a porous block using the crystal growth of calcium sulfate dihydrate, and controlled the pore interconnectivity by limiting the region of crystal growth. The calcium sulfate dihydrate blocks were transformed to bone apatite, carbonate apatite (CO₃Ap) through dissolution–precipitation reactions. Thus, CO₃Ap blocks with 15% and 30% interconnected pore volumes were obtained while maintaining the microarchitecture: they were designated as CO₃Ap-15 and CO₃Ap-30, respectively. At 4 weeks after implantation in a rabbit femur defect, new bone formed throughout CO₃Ap-30, whereas little bone was formed in the center region of CO₃Ap-15. At 12 weeks after implantation, a large portion of CO₃Ap-30 was replaced with new bone and the boundary with the host bone became blurred. In contrast, CO₃Ap-15 remained in the defect and the boundary with the host bone was still clear. Thus, the interconnected pores promote bone ingrowth, followed by replacement of the material with new bone. These findings provide a useful guide for designing bone substitutes for rapid bone regeneration.

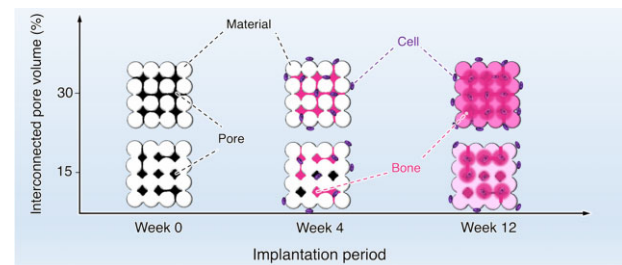
Keywords: bone substitutes; carbonate apatite; pore interconnectivity; bone regeneration

Introduction

Bone defects resulting from severe trauma or wide resection of bone tumors require a graft material for their reconstruction [1–4]. Autografts using the iliac crest, fibula or resected bone after devitalization have been used as an effective option [1, 2, 4]. Although autografting is still regarded as the gold standard for bone reconstruction in post-traumatic conditions [1–3], problems, such as limited tissue mass availability, risk of infection and increased morbidity of the donor site, are unavoidable [5–7]. Therefore, the development of effective bone-substitute materials is urgently needed.

The outcome of bone reconstruction is primarily determined by the chemical composition of the grafting material [8, 9]. Among the bone-substitute materials currently used, carbonate apatite (CO₃Ap), which is the main component of the bone mineral [10–12], has recently attracted much attention owing to its ability to be replaced by new bone during the bone remodeling process, as observed in autografts [13–15]. A much higher osteoconductivity of CO₃Ap was also reported as compared with those of sintered hydroxyapatite (HAp) and β-tricalcium phosphate [16–22].

The architecture of the bone substitutes is also a factor that significantly affects the outcome of bone regeneration [23]. In



particular, porous architectures that increase their specific surface area and vascular permeability are considered essential for the success of reconstruction [23–25]. Although the pore size and volume of the materials typically affect bone ingrowth and formation [26–32], the pore geometry, such as uniformity, orientation and interconnectivity, is also a key design consideration. Notably, an interconnected architecture of pores has been considered effective for the penetration of body fluids and cells, contributing to bone ingrowth. Although the introduction of interconnected pores [2, 23, 33–35] and/or continuous channels [29, 30, 36–40] has been achieved, controlling the pore interconnectivity while maintaining the microarchitecture has not been realized by conventional methods, such as sintering.

Interconnected porous blocks can be fabricated by interconnecting the granules and creating gaps between them. However, in the case of CO₃Ap, the direct interconnection of CO₃Ap granules is difficult because they have no setting ability and sinterability below the decomposition temperature. Therefore, we previously fabricated interconnected porous CO₃Ap blocks by interconnecting precursor granules followed by compositional transformation to CO₃Ap through a dissolution–precipitation reaction; they were interconnected by a thermal fusion with an

Received: September 24, 2021. Revised: January 24, 2022. Accepted: January 30, 2022

© The Author(s) 2022. Published by Oxford University Press.

This is an Open Access article distributed under the terms of the Creative Commons Attribution License (<https://creativecommons.org/licenses/by/4.0/>), which permits unrestricted reuse, distribution, and reproduction in any medium, provided the original work is properly cited.

organic binder [41], the hydrate expansion of CaO granules [42], the setting reaction of α -tricalcium phosphate spheres [43] and the setting reaction of calcium sulfate hemihydrate ($\text{CaSO}_4 \cdot 1/2\text{H}_2\text{O}$) granules [44]. The setting reaction of $\text{CaSO}_4 \cdot 1/2\text{H}_2\text{O}$ granules with water occurs with highly aggressive crystal growth of calcium sulfate dihydrate ($\text{CaSO}_4 \cdot 2\text{H}_2\text{O}$). Although this crystal growth easily causes clogging of gaps between granules and spoiling of the pore interconnectivity of $\text{CaSO}_4 \cdot 2\text{H}_2\text{O}$, we found that this clogging could be avoided by regulating the amount of water [44]. In other words, the pore interconnectivity of the CO_3Ap blocks might be adjustable based on this water removal process.

In this study, we aimed to fabricate CO_3Ap blocks with different pore interconnectivities while maintaining the microarchitecture for histological evaluation. The pore interconnectivity was controlled by limiting the region of crystal growth of $\text{CaSO}_4 \cdot 2\text{H}_2\text{O}$ during the setting reaction. Centrifugal force was used to partially remove water and limit the region of crystal growth. After converting the $\text{CaSO}_4 \cdot 2\text{H}_2\text{O}$ blocks to CO_3Ap through dissolution-precipitation reactions, we implanted the CO_3Ap blocks in the rabbit femur defect to evaluate the influence of pore interconnectivity on bone ingrowth, new bone formation and material resorption.

Materials and methods

Fabrication of CO_3Ap block

In our previous study, a porous CO_3Ap block was fabricated through dissolution-precipitation reactions of a porous calcium sulfate anhydrous (CaSO_4) block, which was obtained by the setting reaction of $\text{CaSO}_4 \cdot 1/2\text{H}_2\text{O}$ granules with water followed by dehydration heat treatment [44]. In this study, we fabricated CO_3Ap blocks with different pore interconnectivities based on this method, with slight modifications.

In brief, commercial $\text{CaSO}_4 \cdot 1/2\text{H}_2\text{O}$ powder (NEW FUJIROCK WHITE, improved dental stone powder, GC Corporation, Tokyo, Japan) was mixed with distilled water at a liquid to powder ratio of $0.2 \text{ cm}^3 \cdot \text{g}^{-1}$ to obtain a set $\text{CaSO}_4 \cdot 2\text{H}_2\text{O}$ block, followed by granulating into the size of 100–200 μm and dehydrating at 120°C for 24 h. The $\text{CaSO}_4 \cdot 1/2\text{H}_2\text{O}$ granules obtained were placed in an acrylic mold (ϕ 6 mm \times 9 mm) with covered stainless steel meshes. Two wetting conditions were used to control the pore interconnectivity: the packed granules were immersed in distilled water for 30 s followed by centrifugation at a speed of $500 \times g$ for 3 min using a tabletop centrifuge (Model 2420, Kubota, Tokyo, Japan), or immersed in distilled water for 30 s without centrifugation. This centrifuge process was designed to remove water except for that retained by interfacial tension with the granules. Both samples were kept inside the mold at room temperature for 24 h to prepare porous $\text{CaSO}_4 \cdot 2\text{H}_2\text{O}$ blocks. The blocks obtained were heat-treated at a heating rate of $1^\circ\text{C} \cdot \text{min}^{-1}$ – 750°C and maintained at 750°C for 6 h. After cooling to room temperature, the blocks were immersed in a $1 \text{ mol} \cdot \text{dm}^{-3}$ solution of Na_2CO_3 (Fuji Film Wako Pure Chemical Corporation, Osaka, Japan) at 60°C for 3 days to convert CaSO_4 into calcium carbonate (CaCO_3). The CaCO_3 blocks obtained were immersed in a $0.1 \text{ mol} \cdot \text{dm}^{-3}$ solution of Na_2HPO_4 (Fuji Film Wako Pure Chemical Corporation) at 60°C for compositional transformation to CO_3Ap . The CO_3Ap blocks obtained from the $\text{CaSO}_4 \cdot 2\text{H}_2\text{O}$ block centrifuged at $500 \times g$ for water removal and those without centrifugation had 30% and 15% interconnected pore volumes, respectively, as shown in the Results and discussion section. Hence, the CO_3Ap blocks derived from the $\text{CaSO}_4 \cdot 2\text{H}_2\text{O}$ block centrifuged at $500 \times g$ and those

without centrifugation are referred to as CO_3Ap -30 and CO_3Ap -15, respectively. The compositional transformation from CaCO_3 to CO_3Ap in a Na_2HPO_4 solution was conducted for 7 (CO_3Ap -30) or 14 days (CO_3Ap -15).

Characterization

The crystal phases of the CO_3Ap blocks were analyzed by powder X-ray diffraction (XRD; D8 Advance diffractometer, Bruker AXS GmbH, Karlsruhe, Germany) with $\text{CuK}\alpha$ radiation generated at an acceleration voltage of 40 kV and a current of 40 mA. The chemical characteristics of the CO_3Ap blocks were analyzed by Fourier transform infrared (FTIR) spectroscopy (FT/IR-6200, JASCO, Tokyo, Japan) using the KBr disk method. The carbonate content in the CO_3Ap blocks was determined by performing the elemental carbon-hydrogen-nitrogen (CHN) analysis (MT-6, Yanako Analytical Instruments, Kyoto, Japan). The remaining sulfate content in the CO_3Ap blocks was assessed by inductively coupled plasma-optical emission spectrometry (ICP-OES, Optima 7300 DV, PerkinElmer, MA, USA).

The surface morphologies of the CO_3Ap blocks were investigated by scanning electron microscopy (SEM; S-3400N, Hitachi High Technologies, Tokyo, Japan) with an acceleration voltage of 10 kV, after being coated with gold-palladium using a magnetron sputtering machine (MSP-1S, Vacuum Device Co., Ibaraki, Japan). Elemental analysis on the fractured surface of the samples was performed by energy-dispersive X-ray (EDX) spectroscopy coupled with the SEM with an accelerating voltage of 15 kV. The volume and size distribution of the interconnected pores in the CO_3Ap blocks were analyzed using mercury intrusion porosimetry (AutoPore 9420, Shimadzu Corporation, Kyoto, Japan). The internal morphology of the CO_3Ap blocks was investigated using the micro-computed tomography (μ -CT) scanning (ScanXmate-L090T, Comscan, Kanagawa, Japan).

The penetrability of the CO_3Ap blocks was evaluated by the infiltration of a 0.05% toluidine blue solution (Fuji Film Wako Pure Chemical Corporation). The block was then immersed in the dye solution for 3 min. The dyed blocks were dried at 60°C for 1 h.

The mechanical strength of the CO_3Ap blocks was evaluated in terms of the compressive strength and diametral tensile strength. After the diameter and height of each block were measured with a micrometer (IP65, Mitutoyo Co., Ltd, Kanagawa, Japan), the block was crushed by a loaded force at a crosshead speed of 1 mm/min using a universal testing machine (Autograph, AGS-J, Shimadzu Corporation). Eight samples per group were analyzed to determine the average compressive strength and diametral tensile strength. The total porosity of the CO_3Ap blocks was determined from their bulk density (determined from each block's weight and volume) and calculated using the theoretical density of HAp ($3.16 \text{ g} \cdot \text{cm}^{-3}$). The apparent porosity of the CO_3Ap blocks was determined according to Archimedes' principle using water as the immersion liquid. Eight samples per group were analyzed to determine the average total porosity and apparent porosity.

The release profiles of calcium and phosphorus were investigated by immersing 100 mm^3 of the CO_3Ap blocks in 5000 mm^3 of 4-(2-hydroxyethyl)-1-piperazineethanesulfonic acid (HEPES) buffer solution (Fuji Film Wako Pure Chemical Corporation) at 37°C . The amount of calcium and phosphorus released was determined by ICP-OES using Optima 7300 DV (PerkinElmer). The HEPES buffer solution was replaced with equal volume of fresh solution every seventh day.

In vitro evaluation

As described in our previous work [45], MC3T3-E1 cells (Riken BioResource Center, Ibaraki, Japan) were maintained in a cell culture medium, which was an alpha modification of Eagle's minimum essential medium (α -MEM; Gibco, USA) supplemented with 10% fetal bovine serum (Gibco), 100 U·cm⁻³ penicillin, 100 mg·cm⁻³ streptomycin and 0.25 mg·cm⁻³ amphotericin B (Gibco). The cells were incubated at 37°C in a humidified atmosphere containing 5% CO₂. For sample preparation for cell invasion assay, each CO₃Ap block (ϕ 6 mm \times 3 mm) was tightly inserted into the edge of an acrylic tube (ϕ 6 mm \times 4 mm) to inhibit free migration of cells along the side of the block. The CO₃Ap blocks inserted in the tubes were placed in a well plate so that one side of the block and tube were in contact with the bottom of the plate. All samples were sterilized in 70% ethanol and rinsed with phosphate buffered saline (PBS). All sterilized samples were immersed in the medium for 1 day to prevent the burst release of calcium ions.

In cell invasion assay, MC3T3-E1 cells were seeded on the samples at an approximate initial concentration of 5.5×10^4 cells·cm⁻³. After 7 days of incubation, the cells attached to the samples were rinsed with PBS and fixed with 4% paraformaldehyde for 15 min. For SEM observation, the cells were dehydrated in a graded ethanol series consisting of 50%, 60%, 70%, 80%, 90% and 99.5% ethanol, and dried by hexamethyldisilazane (Fuji Film Wako Pure Chemical Corporation) before being coated with gold-palladium. For fluorescence staining, the attached cells were permeabilized by immersing the samples in 0.5% Triton X-100 for 15 min. The non-specific reactions were blocked by 60 min of immersion in PBS containing 3% bovine serum albumin at room temperature. F-actins and nuclei of the attached cells were stained with Acti-stain 555 phalloidin (Cytoskeleton Inc., Denver, USA) and Hoechst 33342 (Dojindo, Kumamoto, Japan), respectively. Fluorescence images were captured from the bottom of the samples.

In vivo evaluation

The animal experiments conducted in this study were approved by the Animal Care and Use Committee of Kyushu University (No. A30-293-0; issued 26 November 2018). Eighteen week-old male Japanese white rabbits (Japan SLC, Inc., Shizuoka, Japan) weighing 3.0–3.5 kg were utilized for the experiments. These rabbits were housed at the Center of Biomedical Research, Research Center for Human Disease Modeling, Graduate School of Medical Sciences, Kyushu University. They were maintained on a standard feed and water.

For sample implantation, the rabbits were initially anesthetized via intraperitoneal injection of a mixture of ketamine (30 mg·kg⁻¹) and xylazine (5.0 mg·kg⁻¹). The rear limbs were shaved to remove the fur, and then the skin was disinfected with 10% povidone-iodine (Meiji Seika Pharma Co., Ltd, Tokyo, Japan). The distal epiphysis of the femur was selected as the implant site because of its sufficient bone volume. An incision was made in the skin and periosteum of the femur, and a cylindrical defect (ϕ 6 mm \times 3 mm) was created using a trephine bur. This defect size was adopted based on previous studies [40, 42], in which an effective comparison of material architecture of CO₃Ap was made within 12 weeks without perforating into bone marrow region. It can be noted that this defect size is not generally regarded critical and may not be used for long-term experiments. CO₃Ap-30 or CO₃Ap-15 was implanted into the bone defect, and the periosteum and skin flap were closed ($n=3$ per group). The rabbits were

allowed unrestrained movement in their cages after they recovery from anesthesia. After implantation for 4 and 12 weeks, the rabbits were sacrificed, and the specimens were removed.

The μ -CT images of the specimens were obtained using a μ -CT scanner (SkyScan, Bruker Corporation, MA, USA). For histomorphometric analyses, the specimens were fixed in 10% formalin neutral buffer solution, decalcified with 0.5 mol·dm⁻³ ethylenediaminetetraacetic acid, and embedded in paraffin. The paraffin blocks were sliced at 3- μ m thickness using a sliding microtome (REM-710/CBUH, Yamato Kohki, Asaka, Japan). After deparaffinization, hematoxylin and eosin (HE) staining was performed using a general protocol.

Statistical analysis

Statistical analyses were performed by Tukey's test after one-way ANOVA using R software (The R Foundation for Statistical Computing, ver. 4.0.0, 2020). $P < 0.05$ was considered statistically significant.

Results and discussion

Fabrication and characterization of CO₃Ap blocks

The CO₃Ap blocks derived from the CaSO₄·2H₂O blocks centrifuged at 500 \times g for water removal during the setting reaction (CO₃Ap-30) and those without centrifugation processes (CO₃Ap-15) showed the same XRD patterns, confirming that both were purely composed of apatite without remaining precursors, such as CaSO₄ and CaCO₃ (Fig. 1A). The remaining sulfate groups were not detected from ICP-OES. Furthermore, the FTIR spectra confirmed the presence of carbonate groups and the absence of hydroxyl groups (Fig. 1B). The absorption peaks detected at 1470 and 1420 cm⁻¹ correspond to the substitution of hydroxyl and phosphate groups by carbonate groups (Fig. 1B). Therefore, the apatites obtained were both AB-type CO₃Ap. The CHN analyses showed no significant differences in carbonate content between CO₃Ap-30 and CO₃Ap-15 (Table 1). The carbonate content is equal to that of human bone apatite (6–9 wt%) [12–14].

Both CO₃Ap blocks were cylindrical blocks constructed of granules (Fig. 2A–D). The 2D-sliced images showed a significant difference in the internal architecture (Fig. 2E–H). CO₃Ap-30 showed a pore-interconnected structure throughout the sliced images (Fig. 2E and G). In contrast, CO₃Ap-15 showed less continuous pore interconnections (Fig. 2F and H). The SEM images of the two groups showed a significant difference in surface morphology (Fig. 2I and J). The surface of CO₃Ap-30 exhibited a clear bridging structure of granules (Fig. 2I), while the bridging pattern was smeared out on the surface of CO₃Ap-15 (Fig. 2J). Both CO₃Ap blocks were composed of rod-like crystals (Fig. 2K and L). The surface morphologies observed were consistent with those of CaSO₄·2H₂O blocks, which showed a similar pattern of granular bridging depending on the water removal process (Supplementary Fig. S1). Therefore, the multi-step compositional transformation of the blocks from CaSO₄·2H₂O to CO₃Ap did not alter the macroscopic morphology. The structural difference between CO₃Ap-30 and CO₃Ap-15 is likely to reflect the difference in the crystal growth of CaSO₄·2H₂O. Although the crystal growth of CaSO₄·2H₂O causes expansion in general, free expansion was restricted at the area contacting with the wall of the mold used for filling CaSO₄·1/2H₂O granules. This restricted expansion resulted in a densified structure at the periphery of CaSO₄·2H₂O blocks and CO₃Ap blocks (Fig. 2E–H), as also confirmed by a porosimetry along the diametral direction based on μ -CT images (Supplementary Fig. S2). This densification was more significantly observed in CO₃Ap-15, where

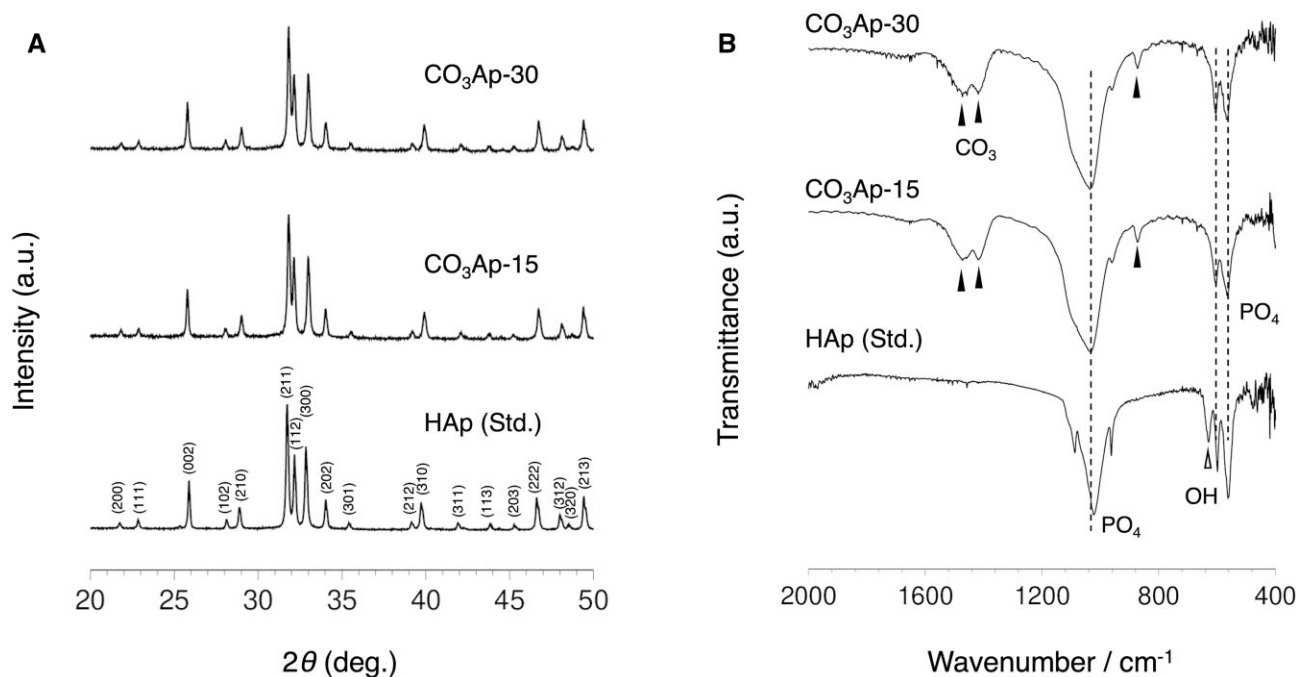


Figure 1. (A) XRD patterns and (B) FTIR spectra of CO₃Ap-30, CO₃Ap-15 and standard HAp. The miller indices of HAp were assigned from PDF# 00-009-0432.

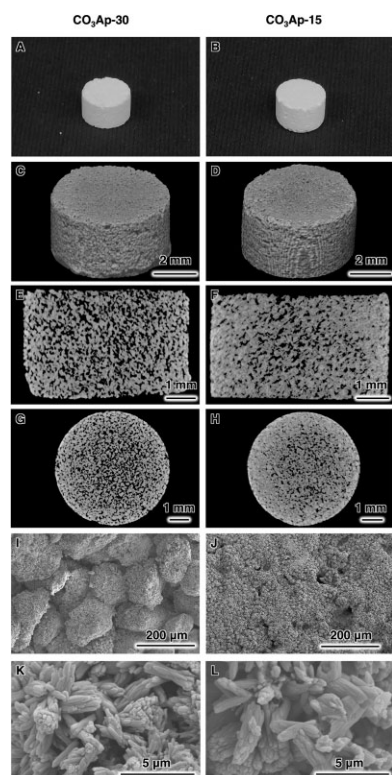


Figure 2. Photograph images of (A) CO₃Ap-30 and (B) CO₃Ap-15. μ -CT scanning observations of materials. μ -CT-based 3D reconstruction images of (C) CO₃Ap-30 and (D) CO₃Ap-15. μ -CT-based sliced images at a sagittal section of (E) CO₃Ap-30 and (F) CO₃Ap-15. μ -CT-based sliced images at a transverse section of (G) CO₃Ap-30 and (H) CO₃Ap-15. SEM images of (I) CO₃Ap-30 and (J) CO₃Ap-15. Magnified SEM images of (K) CO₃Ap-30 and (L) CO₃Ap-15.

much crystal growth occurred. Despite this porosity gradient, the composition of both CO₃Ap blocks was uniform from the outer

Table 1. Carbonate content of CO₃Ap blocks

Sample	Carbonate content (wt%)
CO ₃ Ap-30	7.5 ± 0.5
CO ₃ Ap-15	7.2 ± 0.2

edge to the central region, as confirmed by EDX analysis (Supplementary Fig. S3).

To find quantitative differences in the interconnected porous architecture between CO₃Ap-30 and CO₃Ap-15, mercury intrusion porosimetry was employed (Fig. 3). CO₃Ap-30 showed a larger interconnected pore volume than CO₃Ap-15 (Fig. 3A). Both the CO₃Ap blocks had a pore size distribution at two different scales, namely, larger pores of ~29 μ m (CO₃Ap-30) or 14 μ m (CO₃Ap-15) and smaller pores of ~1 μ m in diameter (Fig. 3B). These larger and smaller pores are likely to originate in the intergranular and intercrystalline gaps of CO₃Ap, respectively. By computing the peak areas of larger pores, the interconnected pore volumes in CO₃Ap-30 and CO₃Ap-15 were determined as 280 and 130 $\text{mm}^3 \cdot \text{g}^{-1}$, respectively. These pore volumes (280 and 130 $\text{mm}^3 \cdot \text{g}^{-1}$) correspond to 30% and 15% of the total volume, respectively.

Pore interconnectivity was visualized using a dye penetration assay (Fig. 4). Complete dye penetration was observed in CO₃Ap-30 showing a stained cross-section, whereas the assay of CO₃Ap-15 resulted in a limited stained area, indicating full and partial pore interconnectivity of CO₃Ap-30 and CO₃Ap-15, respectively. This observation coincides with our previous study, in which the water removal process was identified as the key to creating interconnected pores [44].

There was no significant difference in the mechanical strength and total porosity between CO₃Ap-30 and CO₃Ap-15 (Fig. 5A–C). In other words, the improved pore interconnectivity did not affect the mechanical strength in accordance with the maintained total porosity. Since the equal amount of the starting substance, CaSO₄·1/2H₂O granules were used, both CO₃Ap-30 and CO₃Ap-15

were obtained from the same amount of calcium, resulting in the equal total porosity. In contrast, the apparent porosity of CO₃Ap-30 determined by the Archimedes method was significantly higher than that of CO₃Ap-15, confirming the increased interconnected pores and the reduced closed pores (Fig. 5D). At present, the mechanism necessary to yield an equal mechanical strength while having different pore interconnectivity has not been fully clarified. The mechanical strength is thought to depend mainly on the interlocking degree of CO₃Ap crystals. Although CO₃Ap-30 had a fractured surface with clear granules-fused structure, CO₃Ap-15 exhibited a more disordered fractured surface (Supplementary Fig. S3). Therefore, the CO₃Ap crystals may be also interlocked at the interstitial gaps between granules as well as the intergranular regions, when the crystal growth is

prominent. These two contributions to the mechanical strength may result in an equal mechanical strength with an equal total porosity.

The *in vitro* behaviors of the CO₃Ap blocks were investigated in terms of ion release and cell invasion. During the 28 days of immersion in HEPES buffer, both CO₃Ap-30 and CO₃Ap-15 tended to constantly release calcium and phosphate ions at nearly equivalent rates (Fig. 6). This is consistent with the nearly equal specific surface areas, which were estimated from mercury intrusion porosimetry (CO₃Ap-30: 1.79 m²·g⁻¹; CO₃Ap-15: 1.73 m²·g⁻¹). After 7 days of cell culture, the cells tended to grow preferentially on the top of CO₃Ap-15 surface rather than CO₃Ap-30 surface (Fig. 7A and B). In contrast, no cells were found inside and on the bottom of CO₃Ap-15, while CO₃Ap-30

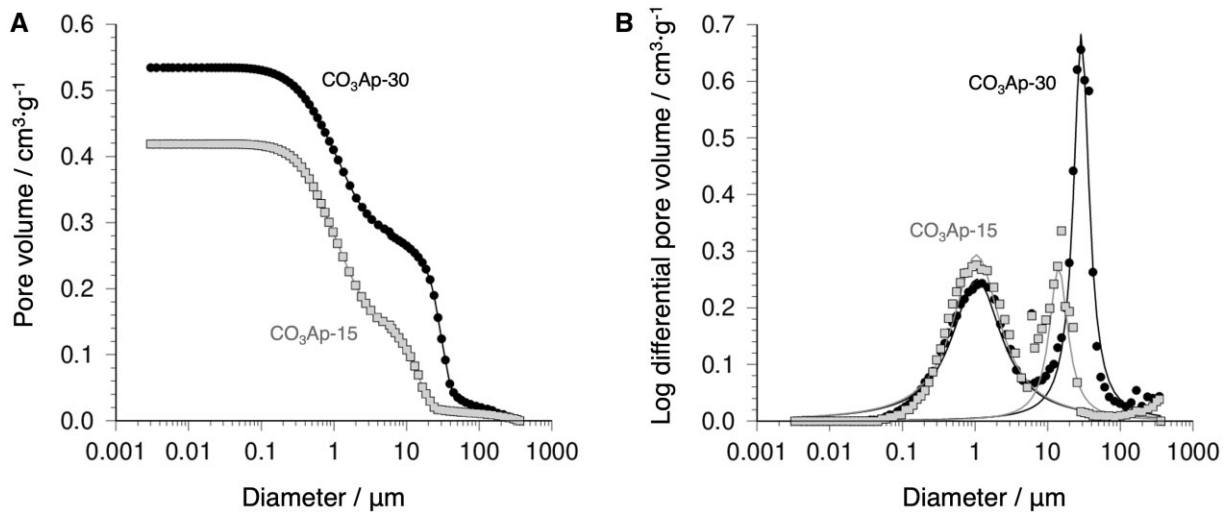


Figure 3. (A) Cumulative and (B) differential pore volume plotted as a function of pore diameter of CO₃Ap-30 and CO₃Ap-15. Differential pattern was best-fitted by two Lorentzian functions.

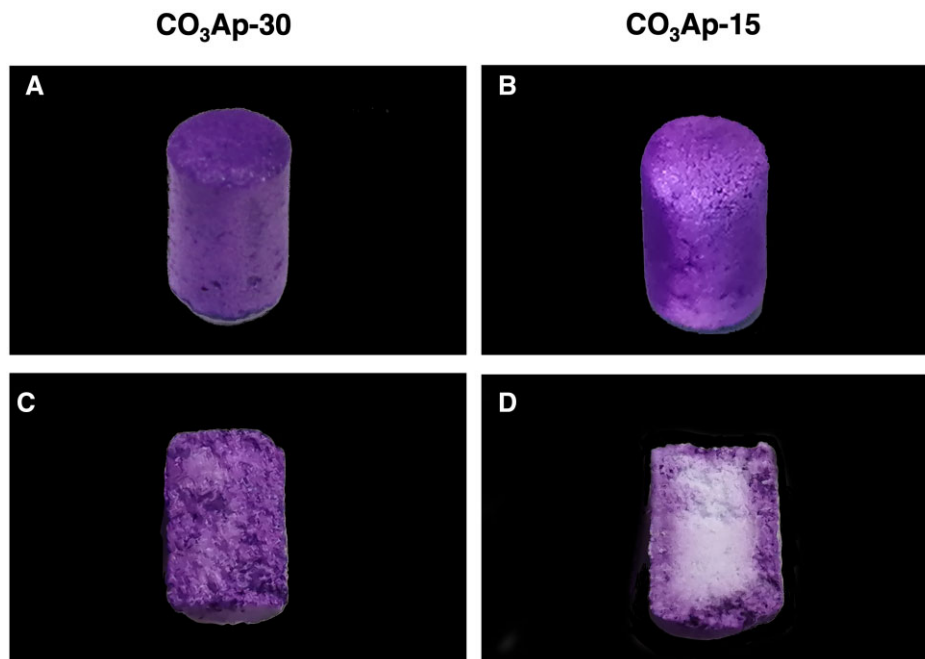


Figure 4. Photograph images of materials after dye penetration assay. Perspective views of (A) CO₃Ap-30 and (B) CO₃Ap-15. Cross-sectional views of (C) CO₃Ap-30 and (D) CO₃Ap-15.

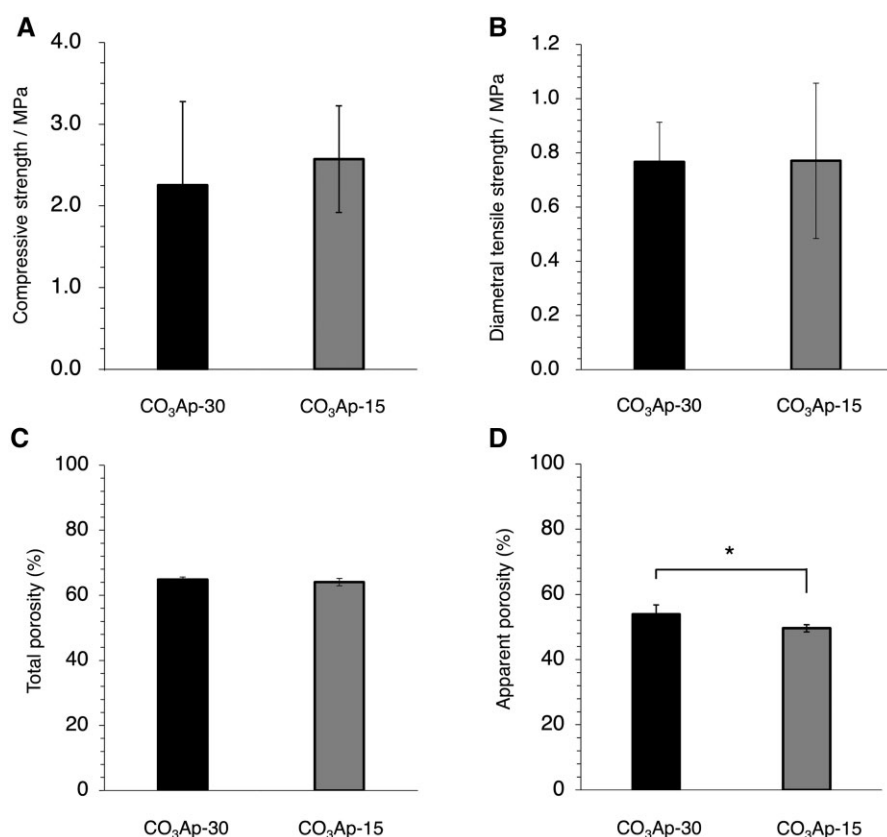


Figure 5. (A) Compressive strength, (B) diametral tensile strength, (C) total porosity and (D) apparent porosity of CO₃Ap-30 and CO₃Ap-15. **P* < 0.05.

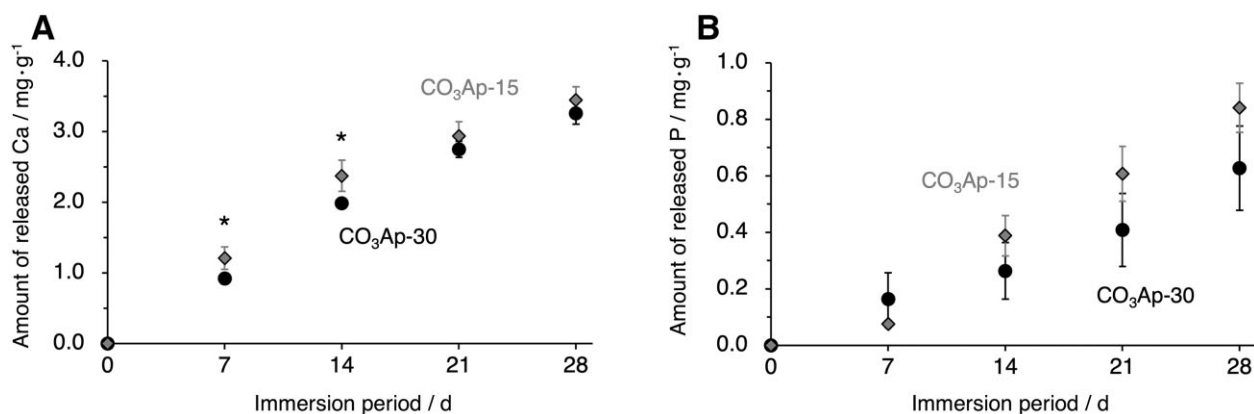


Figure 6. The amount of (A) calcium and (B) phosphorus released from CO₃Ap-30 (black circles) and CO₃Ap-15 (gray diamonds) to the HEPES buffer during 28 days of immersion measured using ICP-OES. **P* < 0.05.

allowed cells to invade to a depth of 3 mm (Fig. 7C–J). Therefore, the difference in pore interconnectivity affected penetration of cells as well as body fluid.

In vivo evaluation

The above characterization of CO₃Ap-30 and CO₃Ap-15 demonstrated that only the pore interconnectivity was distinctly different between the two groups, whereas the chemical composition, micropore distribution, mechanical strength and total porosity were equal. Therefore, the comparison between CO₃Ap-30 and CO₃Ap-15 provides an effective evaluation of the effects associated with pore interconnectivity. Thus,

both the CO₃Ap blocks were implanted in a defect in the rabbit femur.

The μ -CT images showed that at 4 weeks after implantation, CO₃Ap-30 and CO₃Ap-15 remained in the bone defects and maintained their clear boundary with the host bone (Fig. 8A and B). CO₃Ap-30 had a lower CT-positive value in the bone defect and a lower contrast with the host bone. At 12 weeks after implantation, the radiopacity of the defect area decreased in both groups, suggesting that the resorption of CO₃Ap was progressed (Fig. 8C and D). This was accompanied by a diminished dense pattern of implant material, which had been observed during the 4-week period. In the case of CO₃Ap-30 at the 12-week period, the CT-positive value in the defect was fairly close to that of the host

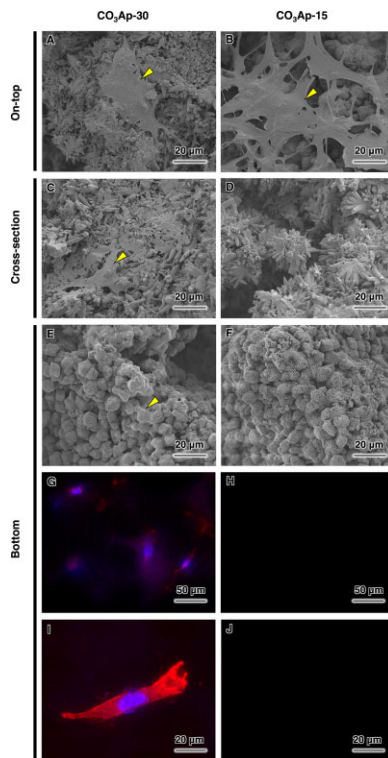


Figure 7. Cell invasion assay of the samples with 3-mm thickness for 7 days of culture period. SEM images at the cell-seeded on-top surface of (A) CO₃Ap-30 and (B) CO₃Ap-15. SEM images at a cross-section of (C) CO₃Ap-30 and (D) CO₃Ap-15. SEM images at the bottom surface of (E) CO₃Ap-30 and (F) CO₃Ap-15. F-actins (red) and nuclei (blue) of attached cells on the bottom surface of (G) CO₃Ap-30 and (H) CO₃Ap-15. Magnified fluorescence images of the bottom surface of (I) CO₃Ap-30 and (J) CO₃Ap-15. Yellow triangles indicate cells.

bone (Fig. 8C). In other words, CO₃Ap-30 had the potential to be resorbed and replaced by cancellous new bone in 12 weeks. In contrast, the remaining material area of CO₃Ap-15 was clearly observed even at the 12-week period (Fig. 8D). Therefore, CO₃Ap-15 was resorbed and replaced by new bone at a slower rate.

To investigate new bone formation, bone ingrowth and material resorption, histological analysis was performed with HE staining. At 4 weeks after implantation, both samples were continuously attached to the host bone without any fibrous tissue, confirming their histocompatibility and osteoconductivity (Fig. 9A and B). Moreover, new bone formed over the entire area inside CO₃Ap-30, whereas the bone area inside CO₃Ap-15 was limited to the region near the host bone. This indicates that interconnected pores in CO₃Ap were easily occupied by new bone due to the absence of barriers for bone ingrowth, while closed pores prevent bone ingrowth into the center region of the material. Osteoblasts, osteoclasts and red blood cells were distributed inside the materials, indicating that the pores were effective for allowing cellular migration and providing an osteoconductive environment (Fig. 9C–H). Even in the area of limited bone formation in CO₃Ap-15 (i.e. the center region), a large number of cells resided, which is thought to be due to the resorption of material by opening the pores that were initially not interconnected (Fig. 9D). Osteoblasts were aligned along the edge of the new bone, while osteoclasts were distributed around the material surfaces (Fig. 9E–H). At 12 weeks after implantation, CO₃Ap-30 and CO₃Ap-15 showed progressed resorption, as manifested in the reduced area of their building granules (Fig. 10A and B). As a morphological change, the CO₃Ap-30-implanted area exhibited a trabecular bone-like pattern consisting of new bone and adipose tissue (Fig. 10A). The boundary between the CO₃Ap-30-implanted area and the surrounding host bone became blurred, while the CO₃Ap-15-implanted area was still clearly distinct from the host bone

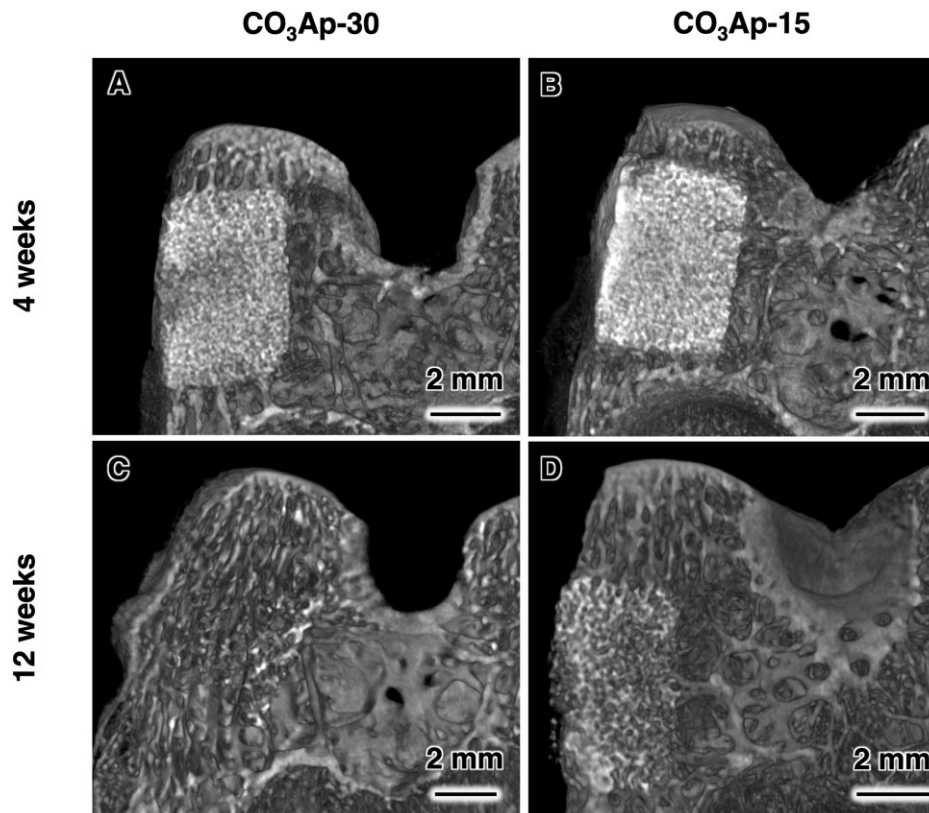


Figure 8. μ -CT images of rabbit femurs with defects reconstructed by grafting CO₃Ap-30 at (A) 4 weeks and (C) 12 weeks after implantation, and CO₃Ap-15 at (B) 4 weeks and (D) 12 weeks after implantation

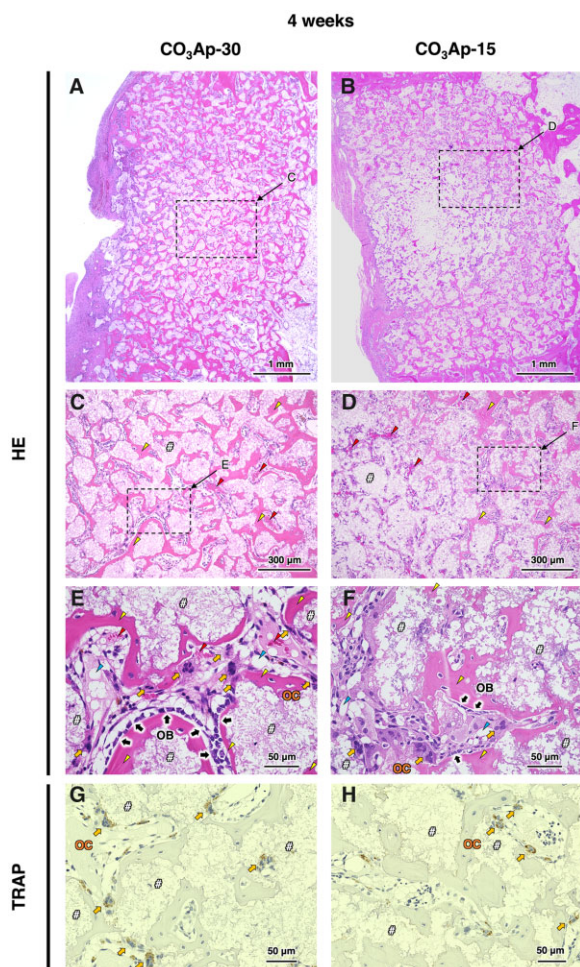


Figure 9. HE-stained histological images of rabbit femurs with defects reconstructed by grafting (A) CO₃Ap-30 and (B) CO₃Ap-15 at 4 weeks after implantation. (C) and (D) show magnified versions of the images presented in (A) and (B), respectively. (E) and (F) show higher magnification images of typical regions in (A) and (B), respectively. (G) and (H) show TRAP-stained images in the region near (E) and (F), respectively. Yellow triangles, red triangles, blue triangles, 'OB', 'OC' and '#' denote new bone, red blood cells, adipose tissues, osteoblasts, osteoclasts and material, respectively.

(Fig. 10A and B). Therefore, CO₃Ap-30 was mostly replaced by cancellous-structured new bone in 12 weeks. In both groups, bone marrow-like tissue as well as adipose tissue was also observed (Fig. 10C and D). Therefore, migration or generation of soft tissue as well as hard tissue became pronounced upon progressed resorption of the material. These soft tissues may have migrated to the bone defect through the bone remodeling. Furthermore, mesenchymal and hematopoietic stem cells, which were thought to have differentiated mainly into osteoblasts and osteoclasts at the 4-week period, may have switched to adipocytes and myelocytes, respectively, to a certain extent. Osteoblasts in an array were observed at the interface between the bone and adipose tissue, while osteoclasts were mainly found near the remaining materials (Fig. 10E–H). Thus, the bone remodeling process governed by the osteoblastic new bone formation and osteoclastic resorption proceeded continuously during the implantation period.

The area percentages of bone and material in the bone defect were calculated from the histological sections (Fig. 11A and B). At 4 weeks after implantation, the bone area inside CO₃Ap-30 was

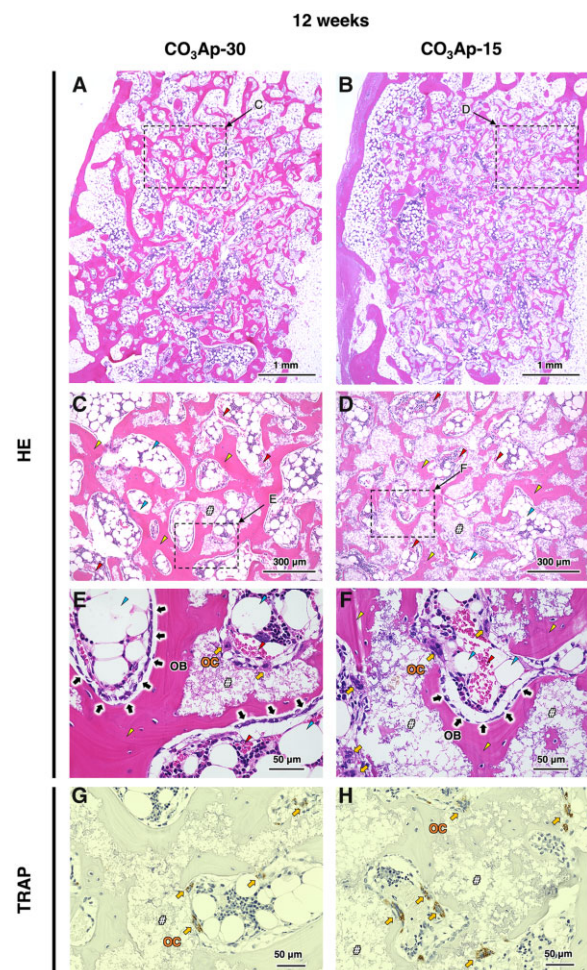


Figure 10. HE-stained histological images of rabbit femurs with defects reconstructed by grafting (A) CO₃Ap-30 and (B) CO₃Ap-15 at 12 weeks after implantation. (C) and (D) show magnified versions of the images presented in (A) and (B), respectively. (E) and (F) show higher magnification images of typical regions in (A) and (B), respectively. (G) and (H) show TRAP-stained images in the region near (E) and (F), respectively. Yellow triangles, red triangles, blue triangles, 'OB', 'OC' and '#' denote new bone, red blood cells, adipose tissues, osteoblasts, osteoclasts and material, respectively.

significantly larger than that inside CO₃Ap-15 (Fig. 11A), corresponding to the observed difference in new bone formation in the region distant from the host bone (Fig. 9A and B). From Weeks 4–12, both groups showed an increase in the bone area, although this was not statistically significant in the case of CO₃Ap-30 (Fig. 11A). Moreover, the material areas drastically decreased at 12 weeks after implantation (Fig. 11B), corresponding to the rapid resorption of CO₃Ap- and replacement by cancellous-structured new bone (Figs 9 and 10).

The above *in vivo* evaluation clearly demonstrates that the interconnectivity of pores has a remarkable influence on new bone formation and material resorption, or CO₃Ap-to-bone remodeling. The pore size of the CO₃Ap blocks used in this study was smaller than that typically adopted. Considering that the pores smaller than 50 μm are usually referred to as micropores [32], both CO₃Ap-30 and CO₃Ap-15, which have larger pores distributed around 29 and 14 μm, respectively, should be referred to as microporous CO₃Ap blocks. Nevertheless, these pores were liquid-penetrable (Fig. 4) and could be occupied by cells through bone ingrowth (Figs 9 and 10). Therefore, although quite small,

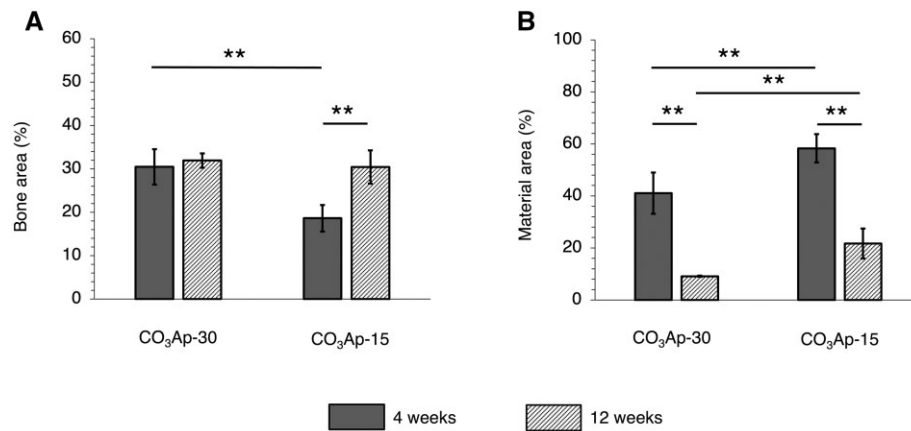


Figure 11. Area percentages of (A) bone and (B) remaining material in each bone defect. ** $P < 0.01$.

the pores distributed around 29 and 14 μm acted as a penetrable space for bony tissue, similar to macropores. Typically, the effects of macropore size have been associated with angiogenesis, which is in competition with the ingrowth of fibrous tissue [28, 30]. Correspondingly, the osteoconductivity evaluated by the bone area decreased below a certain threshold of pore size ($\sim 500 \mu\text{m}$) [27]. From a geometrical point of view, osteoconductivity should also be affected by pore geometry, even at the same pore size and volume. For example, the lower threshold of the effective pore size was decreased to $\sim 300 \mu\text{m}$ by using a uniformly oriented honeycomb CO₃Ap blocks [29, 30]. In this study, we used a CO₃Ap block with fully interconnected pores smaller than 100 μm in diameter, and achieved almost complete replacement of the implanted material with new bone in 12 weeks (Fig. 10A, C and E). Therefore, 3D porous architectures with high pore interconnectivity are associated with rapid bone regeneration, which may drastically shorten hospitalization. Furthermore, upon significant resorption of the material, bone marrow-like tissues were observed at the 12-week period (Fig. 10). A detailed mechanism is currently not available. Similarly, a previous investigation using honeycombed CO₃Ap reported the generation of bone marrow-like tissue upon progressed resorption of CO₃Ap with a high micropore volume, which might be associated with an elevated local Ca²⁺ concentration [46]. As shown in the porosimetry results, both the CO₃Ap blocks prepared in this study had a micropore volume of more than 50% of the pore volume (Fig. 3). Considering that even interconnected pores were smaller than 100 μm , the overall volume occupied by micropores was extremely large. Therefore, further studies are needed to understand the tissue reactions that generate bone marrow-like tissues using highly microporous architectures.

Conclusions

The CO₃Ap blocks with 15% and 30% interconnected pore volumes, i.e. CO₃Ap-15 and CO₃Ap-30, for histological evaluation of the rabbit femur defect were fabricated in this study. Other structural parameters, such as microporosity, micropore size and total porosity, were equal between CO₃Ap-15 and CO₃Ap-30. The fabrication of CO₃Ap-30 was achieved by a centrifuge method to limit the region of crystal growth of CaSO₄·2H₂O, followed by compositional transformation to CO₃Ap. At the 4-week period, new bone formed over the entire region of CO₃Ap-30, whereas a much more scarce formation of bone in the center region of CO₃Ap-15 was

observed. Therefore, the rate of bone ingrowth was significantly affected by the pore interconnectivity. At the 12-week period, the original block morphology of CO₃Ap-30 mostly vanished upon replacement by cancellous-structured new bone, whereas CO₃Ap-15 remained in the bone defect. From this observation, we conclude that introducing interconnected pores is a highly effective approach for realizing rapid bone regeneration by allowing earlier bone ingrowth, followed by replacement of the material with new bone.

Supplementary data

Supplementary data are available at REGGIO online.

Funding

This research was supported, in part, by Japan Agency for Medical Research and Development under Grant Number JP20im0502004, Grant-in-Aid for Research Activity start-up (18H06295) and Grant-in-Aid for Early-Career Scientists (20K18576) from Japan Society for the Promotion of Science.

Author contributions

M.E. carried out the preparation and characterization of materials, participated in the design of the study and analyzed *in vivo* experimental results; R.K. wrote the manuscript, conducted *in vitro* and *in vivo* experiments, carried out the characterization of materials and supervised the study; K.H. critically reviewed the manuscript and participated in the design of the study; A.T. participated in the design of the study; M.S. conducted *in vitro* experiments and critically reviewed the manuscript; K.I. conceived and designed the experiments, critically reviewed the manuscript and supervised the study.

Conflict of interest statement. None declared.

References

- García-Gareta E, Coathup MJ, Blunn GW. Osteoinduction of bone grafting materials for bone repair and regeneration. *Bone* 2015;81:112–21.
- Calori GM, Mazza E, Colombo M, Ripamonti C. The use of bone-graft substitutes in large bone defects: any specific needs? *Injury* 2011;42:S56–63.

3. Wang W, Yeung KW. Bone grafts and biomaterials substitutes for bone defect repair: a review. *Bioact Mater* **2017**;2:224–47.
4. Panagopoulos GN, Mavrogenis AF, Mauffrey C, Lesenský J, Angelini A, Megaloikononimos PD, Igoumenou VG, Papanastassiou J, Savvidou O, Ruggieri P, Papagelopoulos PJ. Intercalary reconstructions after bone tumor resections: a review of treatments. *Eur J Orthop Surg Traumatol* **2017**;27:737–46.
5. Arrington ED, Smith WJ, Chambers HG, Bucknell AI, Davino NA. Complications of iliac crest bone graft harvesting. *Clin Orthop Relat Res* **1996**;329:300–9.
6. Sakkas A, Schramm A, Winter K, Wilde F. Risk factors for post-operative complications after procedures for autologous bone augmentation from different donor sites. *J Cranio Maxillofac Surg* **2018**;46:312–22.
7. Takamoto M, Takechi M, Ohta K, Ninomiya Y, Ono S, Shigeishi H, Tada M, Kamata N. Risk of bacterial contamination of bone harvesting devices used for autogenous bone graft in implant surgery. *Head Face Med* **2013**;9:3.
8. Yamasaki N, Hirao M, Nanno K, Sugiyasu K, Tamai N, Hashimoto N, Yoshikawa H, Myoui A. A comparative assessment of synthetic ceramic bone substitutes with different composition and microstructure in rabbit femoral condyle model. *J Biomed Mater Res B Appl Biomater* **2009**;91:788–98.
9. Ghanaati S, Barbeck M, Detsch R, Deisinger U, Hilbig U, Rausch V, Sader R, Unger RE, Ziegler G, Kirkpatrick CJ. The chemical composition of synthetic bone substitutes influences tissue reactions *in vivo*: histological and histomorphometrical analysis of the cellular inflammatory response to hydroxyapatite, beta-tricalcium phosphate and biphasic calcium phosphate ceramics. *Biomed Mater* **2012**;7:015005.
10. LeGeros RZ, Trautz OR, LeGeros JP. Apatite crystallites: effects of carbonate on morphology. *Science* **1967**;155:1409–11.
11. LeGeros RZ. *Calcium Phosphates in Oral Biology and Medicine*. New York: Karger, **1991**.
12. Hassan AA, Termine JD, Haynes CV. Mineralogical studies on bone apatite and their implications for radiocarbon dating. *Radiocarbon* **1977**;19:364–74.
13. Ishikawa K. Bone substitute fabrication based on dissolution–precipitation reactions. *Materials (Basel)* **2010**;3:1138–55.
14. Ishikawa K. Carbonate apatite bone replacement: learn from the bone. *J Ceram Soc Japan* **2019**;127:595–601.
15. Nakagawa T, Kudoh K, Fukuda N, Kasugai S, Tachikawa N, Koyano K, Matsushita Y, Sasaki M, Ishikawa K, Miyamoto Y. Application of low-crystalline carbonate apatite granules in 2-stage sinus floor augmentation: a prospective clinical trial and histomorphometric evaluation. *J Periodontal Implant Sci* **2019**;49:382–96.
16. Nagai H, Fujioka-Kobayashi M, Fujisawa K, Ohe G, Takamaru N, Hara K, Uchida D, Tamatani T, Ishikawa K, Miyamoto Y. Effects of low crystalline carbonate apatite on proliferation and osteoblastic differentiation of human bone marrow cells. *J Mater Sci Mater Med* **2015**;26:99–107.
17. Ishikawa K, Miyamoto Y, Tsuchiya A, Hayashi K, Tsuru K, Ohe G. Physical and histological comparison of hydroxyapatite, carbonate apatite, and β -tricalcium phosphate bone substitutes. *Materials* **2018**;11:1993.
18. Mano T, Akita K, Fukuda N, Kamada K, Kurio N, Ishikawa K, Miyamoto Y. Histological comparison of three apatitic bone substitutes with different carbonate contents in alveolar bone defects in a beagle mandible with simultaneous implant installation. *J Biomed Mater Res B Appl Biomater* **2020**;108:1450–9.
19. Sato N, Handa K, Venkataiah VS, Hasegawa T, Njuguna MM, Yahata Y, Saito M. Comparison of the vertical bone defect healing abilities of carbonate apatite, β -tricalcium phosphate, hydroxyapatite and bovine-derived heterogeneous bone. *Dent Mater J* **2020**;39:309–18.
20. Kanazawa M, Tsuru K, Fukuda N, Sakemi Y, Nakashima Y, Ishikawa K. Evaluation of carbonate apatite blocks fabricated from dicalcium phosphate dihydrate blocks for reconstruction of rabbit femoral and tibial defects. *J Mater Sci Mater Med* **2017**;28:85–95.
21. Ayukawa Y, Suzuki Y, Tsuru K, Koyano K, Ishikawa K. Histological comparison in rats between carbonate apatite fabricated from gypsum and sintered hydroxyapatite on bone remodeling. *BioMed Res Int* **2015**;2015:579541.
22. Hayashi K, Kishida R, Tsuchiya A, Ishikawa K. Granular honeycombs composed of carbonate apatite, hydroxyapatite, and β -tricalcium phosphate as bone graft substitutes: effects of composition on bone formation and maturation. *ACS Appl Bio Mater* **2020**;3:1787–95.
23. Bobbert FSL, Zadpoor AA. Effects of bone substitute architecture and surface properties on cell response, angiogenesis, and structure of new bone. *J Mater Chem B* **2017**;5:6175–92.
24. Karageorgiou V, Kaplan D. Porosity of 3D biomaterial scaffolds and osteogenesis. *Biomaterials* **2005**;26:5474–91.
25. Hannink G, Arts JJC. Bioresorbability, porosity and mechanical strength of bone substitutes: what is optimal for bone regeneration? *Injury* **2011**;42:S22–5.
26. Tsuruga E, Takita H, Itoh H, Wakisaka Y, Kuboki Y. Pore size of porous hydroxyapatite as the cell-substratum controls BMP-induced osteogenesis. *J Biochem* **1997**;121:317–24.
27. Gauthier O, Bouler JM, Aguado E, Pilet P, Daculsi G. Macroporous biphasic calcium phosphate ceramics: influence of macropore diameter and macroporosity percentage on bone ingrowth. *Biomaterials* **1998**;19:133–9.
28. Feng B, Jinkang Z, Zhen W, Jianxi L, Jiang C, Jian L, Guolin M, Xin D. The effect of pore size on tissue ingrowth and neovascularization in porous bioceramics of controlled architecture *in vivo*. *Biomed Mater* **2011**;6:015007.
29. Hayashi K, Munar ML, Ishikawa K. Effects of macropore size in carbonate apatite honeycomb scaffolds on bone regeneration. *Mater Sci Eng C Mater Biol Appl* **2020**;111:110848.
30. Hayashi K, Ishikawa K. Honeycomb scaffolds fabricated using extrusion molding and the sphere-packing theory for bone regeneration. *ACS Appl Bio Mater* **2021**;4:721–30.
31. Levengood SKL, Polak SJ, Wheeler MB, Maki AJ, Clark SG, Jamison RD, Johnson AJW. Multiscale osteointegration as a new paradigm for the design of calcium phosphate scaffolds for bone regeneration. *Biomaterials* **2010**;31:3552–63.
32. Hayashi K, Ishikawa K. Effects of nanopores on the mechanical strength, osteoclastogenesis, and the osteogenesis in honeycomb scaffolds. *J Mater Chem B* **2020**;8:8536–45.
33. Osborn JF, Newesely H. The material science of calcium phosphate ceramics. *Biomaterials* **1980**;1:108–11.
34. Blokhuis TJ, Termaat MF, den Boer FC, Patka P, Bakker FC, Haarman HJTM. Properties of calcium phosphate ceramics in relation to their *in vivo* behavior. *J Trauma Acute Care Surg* **2000**;48:179–86.
35. Mastrogiacomo M, Scaglione S, Martinetti R, Dolcini L, Beltrame F, Cancedda R, Quarto R. Role of scaffold internal structure on *in vivo* bone formation in macroporous calcium phosphate bioceramics. *Biomaterials* **2006**;27:3230–7.

36. Kang Y, Chang J. Channels in a porous scaffold: a new player for vascularization. *Regen Med* **2018**;13:705–15.
37. Yu T, Liu Q, Jiang T, Wang XS, Yang YZ, Kang YQ. Channeled β -TCP scaffolds promoted vascularization and bone augmentation in mandible of beagle dogs. *Adv Funct Mater* **2016**;26:6719–27.
38. Sakemi Y, Hayashi K, Tsuchiya A, Nakashima Y, Ishikawa K. Reconstruction of critical-size segmental defects in rat femurs using carbonate apatite honeycomb scaffolds. *J Biomed Mater Res A* **2021**;109:1613–22.
39. Hayashi K, Kishida R, Tsuchiya A, Ishikawa K. Honeycomb blocks composed of carbonate apatite, β -tricalcium phosphate, and hydroxyapatite for bone regeneration: effects of composition on biological responses. *Mater Today Bio* **2019**;4:100031.
40. Hayashi K, Kato N, Kato M, Ishikawa K. Impacts of channel direction on bone tissue engineering in 3D-printed carbonate apatite scaffolds. *Mater Des* **2021**;204:109686.
41. Putri TS, Hayashi K, Ishikawa K. Fabrication of three-dimensional interconnected porous blocks composed of robust carbonate apatite frameworks. *Ceram Int* **2020**;46:20045–9.
42. Tanaka K, Tsuchiya A, Ogino Y, Koyano K, Ishikawa K. Fabrication and histological evaluation of a fully interconnected porous CO_2Ap block formed by hydrate expansion of CaO granules. *ACS Appl Bio Mater* **2020**;3:8872–8.
43. Ishikawa K, Arifta TI, Hayashi K, Tsuru K. Fabrication and evaluation of interconnected porous carbonate apatite from alpha tricalcium phosphate spheres. *J Biomed Mater Res B Appl Biomater* **2019**;107:269–77.
44. Kishida R, Elsheikh M, Hayashi K, Tsuchiya A, Ishikawa K. Fabrication of highly interconnected porous carbonate apatite blocks based on the setting reaction of calcium sulfate hemihydrate granules. *Ceram Int* **2021**;47:19856–63.
45. Shimabukuro M, Hayashi K, Kishida R, Tsuchiya A, Ishikawa K. No-observed-effect level of silver phosphate in carbonate apatite artificial bone on initial bone regeneration. *ACS Infect Dis* **2022**;8:159–69.
46. Hayashi K, Kishida R, Tsuchiya A, Ishikawa K. Carbonate apatite micro-honeycombed blocks generate bone marrow-like tissues as well as bone. *Adv Biosyst* **2019**;3:1900140.